

Anomalous thermal properties and spin crossover of ferromagnesite (Mg,Fe)CO₃

Han Hsu,^{1,*} C . Crisostomo,¹ Wenzhong Wang,² and Zhongqing Wu²

¹*Department of Physics, National Central University, Taoyuan City 32001, Taiwan*

²*School of Earth and Space Sciences,*

University of Science and Technology of China, Hefei, Anhui 230026, P. R. China

(Dated: September 1, 2022)

Abstract

Ferromagnesite [(Mg_{1-x}Fe_x)CO₃], also referred to as magnesiosiderite at high iron concentration ($x > 0.5$), is a solid solution of magnesite (MgCO₃) and siderite (FeCO₃). Ferromagnesite is believed to enter the Earth's lower mantle via subduction and is considered as a major carbon carrier in the Earth's lower mantle, playing a key role in the Earth's deep carbon cycle. Experiments have shown that ferromagnesite undergoes a pressure-induced spin crossover, accompanied by volume and elastic anomalies, in the lower-mantle pressure range. In this work, we investigate thermal properties of (Mg_{1-x}Fe_x)CO₃ ($0 < x \leq 1$) using first-principles calculations. We show that nearly all thermal properties of ferromagnesite are drastically altered by iron spin crossover, including anomalous reduction of volume, anomalous softening of bulk modulus, and anomalous increases of thermal expansion, heat capacity, and Grüneisen parameter. Remarkably, the anomaly of heat capacity remains prominent (up to $\sim 40\%$) at high temperature without smearing out, which suggests that iron spin crossover may significantly affect the thermal properties of subducting slabs and the Earth's deep carbon cycle.

* Corresponding author: hanhsu@ncu.edu.tw

I. INTRODUCTION

Ferromagnesite $[(\text{Mg}_{1-x}\text{Fe}_x)\text{CO}_3]$, also referred to as magnesiosiderite at high iron concentration ($x > 0.5$), is a solid solution of magnesite (MgCO_3) and siderite (FeCO_3), both crystallizing in $R\bar{3}c$ symmetry (space group No. 167) at ambient conditions. Ferromagnesite is believed to enter the Earth’s lower mantle (660–2890 km deep, pressure range 23–135 GPa) via subduction and is considered as a major carbon carrier in the Earth’s lower mantle, playing a key role in the Earth’s deep carbon cycle [1, 2]. Experiments have shown that ferromagnesite remains stable up to 115 GPa and 1300–3000 K (depending on pressure, iron concentration, and iron spin state) [3–5]. Beyond the above-mentioned pressure (P) and temperature (T) range, ferromagnesite undergoes various complicated structural transitions and redox reactions, depending on iron concentration. Orthorhombic, monoclinic, and triclinic phases of $(\text{Mg,Fe})\text{CO}_3$, and Fe^{3+} -bearing $\text{Mg}_2\text{Fe}_2\text{C}_4\text{O}_{13}$, $\text{Fe}_4\text{C}_4\text{O}_{13}$, and $\text{Fe}_4\text{C}_3\text{O}_{12}$ have been proposed based on experiments [3–9] and first-principles calculations [10–13], and consensus has not been reached. Clearly, iron directly affects the properties of (Fe,Mg) -bearing carbonates, including their structural transitions and phase boundaries.

One more complexity of ferromagnesite arises from iron spin crossover (SCO), also referred to as spin transition: The total electron spin (S_{el}) of iron varies with pressure and temperature. At ambient conditions, Fe^{2+} in ferromagnesite adopts the high-spin (HS, $S_{el} = 2$) state; upon compression, S_{el} decreases. Signatures of SCO in ferromagnesite have been observed via various spectroscopic techniques, including x-ray emission [14] and absorption [15], Mössbauer [15], Raman [15–21], and optical absorption spectroscopy [22–24]. In addition, volume and elastic anomalies accompanying SCO have been observed via x-ray diffraction [16, 17, 25–29] and Brillouin scattering [30, 31] experiments, respectively. In the above-mentioned room-temperature ($T = 300$ K) experiments, SCO typically starts at 40–49 GPa and finishes at 46–56 GPa; the typical width of the SCO region is 5–10 GPa. An exception is observed via Mössbauer spectroscopy, indicating an SCO region of 52–61 GPa [15]. Our previous *static* calculation has confirmed that only the HS and the low-spin (LS, $S_{el} = 0$) states are involved in the SCO of ferromagnesite, while the intermediate-spin (IS, $S_{el} = 1$) state is highly unlikely [32]. The HS–LS SCO region and volume anomaly given by our calculation are also in good agreement with experiments [32]. So far, most experimental studies for the SCO of ferromagnesite are conducted at room temperature; studies for

the thermal properties at high P – T conditions have been scarce [29], despite their importance to fully understand the SCO of ferromagnesite in the Earth’s interior and its potential geophysical and geochemical effects.

In a broader perspective, iron is incorporated in many minerals in the Earth’s interior, including ferropericlase [(Mg,Fe)O] and Fe-bearing bridgmanite (MgSiO₃ perovskite), which constitute ~ 20 and ~ 75 vol% of the Earth’s lower mantle, respectively. Extensive studies on these two minerals have shown that SCO directly affects the physical properties of the host minerals and also affects iron diffusion and partitioning in the Earth’s interior (see Refs. 33–36 for review). SCO of ferropericlase is now known to control the structure of the large low velocity provinces [37] and to generate the anticorrelation between bulk sound and shear velocities in the lower mantle [38]. Further geophysical and geochemical effects of SCO have been anticipated [35, 36]. In addition to ferropericlase, bridgmanite, and ferromagnesite, a few more minerals of potential geophysical and geochemical importance have also been reported to undergo SCO, including Fe-bearing new hexagonal aluminous (NAL) phase NaMg₂(Si,Al)₆O₁₂ [39–41], calcium-ferrite aluminous (CF) phase (Na,Mg)(Si,Al)₂O₄ [42], and pyrite-type FeO₂H_{*y*} ($0 \leq y \leq 1$) [43, 44]. Despite a variety of mantle minerals are subject to SCO, studies for their thermal properties during SCO at high P – T conditions have been scarce. Recently, anomalous changes of thermal conductivity during SCO have been observed in ferromagnesite [21], ferropericlase [45, 46], and bridgmanite [47, 48] via pulsed light heating thermorefectance and time-domain thermorefectance (TDTR) experiments. In these TR-based experiments, either thermal diffusivity [45, 48] or thermal effusivity [46, 47] are measured. To extract thermal conductivity from TR-based experiments, heat capacity is a necessary input [49, 50]. In practice, since heat capacities at high P – T conditions are not easily available, estimated values are often adopted [46, 47]. This approach, however, may lead to inaccurate estimate of thermal conductivity, as the anomalous change of heat capacity during SCO (see Sec. III and Ref. 51) is ignored. A comprehensive computational study is thus desirable, to provide necessary information for the analysis of TR-based experiments, and to further shed light on the thermal properties of ferromagnesite and related materials during SCO at high P – T conditions.

II. COMPUTATIONAL METHOD

In this work, all calculations are performed using the QUANTUM ESPRESSO codes [52]; ultrasoft pseudopotentials (USPPs) generated with the Vanderbilt method [53] are adopted. To properly treat the on-site Coulomb interaction of Fe-3d electrons, we use the local density approximation + self-consistent Hubbard U (LDA+ U_{sc}) method, with the U parameters computed self-consistently [54–57]. Via LDA+ U_{sc} calculations, SCO (or the lack thereof) in ferropericlaase, bridgmanite, MgSiO₃ post-perovskite, ferromagnesite, and the NAL phase have been successfully elucidated [32, 41, 58–62]. Here we adopt the previously reported $U_{sc} = 4.0$ and 5.4 eV for the HS and LS Fe²⁺, respectively [32]. Structural optimizations for (Mg_{1-x}Fe_x)CO₃ with $x = 0.125$ and with $x = 0.5$ or 1 are performed using 40 and 10-atom cells, respectively, as shown in Fig. 1. Phonon calculations are performed using the Phonopy package, in which finite-displacement method is implemented [63]. Within this method, we adopt supercells containing up to 270 (for $x = 0.5$ and 1) or 320 (for $x = 0.125$) atoms. With the phonon spectra $\omega_{\nu\mathbf{q}}^i(V)$ of spin state i ($i = \text{HS, IS, or LS}$) at volume V obtained, we compute the vibrational free energy $F_i^{vib}(T, V)$ within the quasi-harmonic approximation (QHA); the equation of state $V_i(P, T)$, Gibbs free energy $G_i(P, T)$, and other thermal parameters of spin state i can be determined accordingly, as detailed in the Supplemental Materials (SM) [64]. We fit our calculation results with the third-order Birch–Murnaghan equation of state (3rd BM EoS) using the qha Python package [65].

At nonzero temperatures ($T \neq 0$), ferromagnesite goes through a mixed-spin (MS) phase/state, in which all spin states coexist. The fraction of spin state i in the MS phase is written as $n_i = n_i(P, T)$. For ferromagnesite, the IS state is energetically *unfavorable*, and the IS fraction n_{IS} is negligible [32]. Effectively, $n_{IS} = 0$, and $n_{LS} + n_{HS} = 1$. For convenience, we write $n_{LS} \equiv n$ and $n_{HS} = 1 - n$. Based on the thermodynamic model detailed in the SM [64], the LS fraction $n(P, T)$ is given by

$$n = \frac{1}{1 + \exp(-\Delta G_{LS}/k_B T)}, \quad (1)$$

where $\Delta G_{LS} \equiv G_{LS} - G_{HS}$. With known LS fraction, the Gibbs free energy $G(P, T)$ of the MS phase can be written, from which all thermal parameters of the MS phase can be derived (see the SM [64]).

III. RESULTS

To analyze the lattice vibration of $(\text{Mg}_{1-x}\text{Fe}_x)\text{CO}_3$, we plot the vibrational density of states (VDOS) of MgCO_3 and $(\text{Mg}_{0.5}\text{Fe}_{0.5})\text{CO}_3$ at $V = 37.01 \text{ \AA}^3/\text{f.u.}$, as shown in Fig. 2. At this volume, Mg atoms contribute to the vibrational modes in the region of 0–20 THz (0–667 cm^{-1}) [Fig. 2(a)]; HS Fe contributes mostly to the region of 3–8 THz (100–267 cm^{-1}) [Fig. 2(b)]; LS Fe contributes to the region of 0–20 THz (0–667 cm^{-1}), and its projected VDOS is nearly the same as Mg [Fig. 2(c)]. Such dependence of atomic vibration on iron spin state indicates that the interatomic force constants (IFCs) between HS Fe and neighboring atoms are, in average, smaller than the IFCs between LS Fe and neighboring atoms. As a consequence, HS $(\text{Mg,Fe})\text{CO}_3$ has a smaller bulk modulus and larger heat capacity than LS $(\text{Mg,Fe})\text{CO}_3$ (see later in Figs. 4 and 7). For ferromagnesite, only the HS and LS states are relevant [32]; a spin phase diagram can be obtained by plotting the LS fraction $n(P, T)$. Figure 2(d) is the spin phase diagram of $(\text{Mg}_{0.5}\text{Fe}_{0.5})\text{CO}_3$, where the LS fraction is indicated by color. Here, we use the white color to indicate $n = 0.5$, which is equivalent to $\Delta G_{LS} = 0$ [see Eq. (1)]. The white color thus also marks the spin-transition pressure P_t and the boundary between the HS and LS states. Evidently, $(\text{Mg}_{0.5}\text{Fe}_{0.5})\text{CO}_3$ undergoes a sharp HS–LS transition with a very narrow SCO region at low temperature. As the temperature increases, the width of the SCO region is broadened, the sharp spin transition becomes a smoother and broader SCO, and the spin-transition pressure P_t increases.

To better analyze the spin phase diagram of $(\text{Mg}_{1-x}\text{Fe}_x)\text{CO}_3$, we plot the isothermal LS fraction $n(P)$ for $T = 300, 600$, and 1200 K in Fig. 3. This choice of temperature is based on experimental results: $(\text{Mg}_{1-x}\text{Fe}_x)\text{CO}_3$ with $x \geq 0.65$ is stable up to $T \sim 1300 \text{ K}$ when $P \gtrsim 50 \text{ GPa}$ [4, 5]. Here, we also investigate the effects of iron concentration by considering $x = 0.125, 0.5$, and 1 , as shown in Figs. 3(a)–3(c), respectively. Noticeably, the $n(P)$ curves for all three x 's are nearly the same, indicating that iron concentration barely affects the spin phase diagram. In contrast, for ferropericlase $(\text{Mg}_{1-x}\text{Fe}_x)\text{O}$, the spin-transition pressure P_t significantly increases with x when $0.25 \leq x \leq 1$ [35, 36]. Given such characteristic of $(\text{Mg}_{1-x}\text{Fe}_x)\text{CO}_3$, its SCO can be exemplified by the case of $x = 0.5$ [Fig. 3(b)]: At $T = 300, 600$, and 1200 K , $P_t = 57, 62$, and 73 GPa , and the widths of the SCO regions are $\sim 10, \sim 24$, and $\sim 45 \text{ GPa}$, respectively. Clearly, the computed $n(P)$ for $T = 300 \text{ K}$ is in good agreement with room-temperature experiments reviewed in Sec. I. In

Figs. 3(d)–3(f) and 3(g)–3(i), we plot the derivatives of $n(P, T)$ with respect to pressure and temperature, respectively, for their direct relevance to the anomalous changes of the bulk modulus and thermal expansivity, respectively, as shall be discussed later. Noticeably, as the temperature increases, the peaks of $\partial n/\partial P$ and the dips of $\partial n/\partial T$ are broadened, and their magnitudes are reduced.

In Figs. 4(a)–4(c), we plot the compression curves $V(P)$ of $(\text{Mg}_{1-x}\text{Fe}_x)\text{CO}_3$ in the MS phase for iron concentrations $x = 0.125, 0.5$, and 1 , respectively. Compression curves of the pure HS and LS states (V_{HS} and V_{LS}) are also included for reference. As the iron concentration x increases, V_{HS} shifts up while V_{LS} shifts down. This is because the ionic radius of the HS/LS Fe^{2+} is larger/smaller than that of Mg^{2+} . By comparing $V(P)$ of the MS phase with the LS fraction $n(P)$ shown in Fig. 3(a)–3(c), one can notice that (1) before and after the SCO, $V(P)$ merges with V_{HS} and V_{LS} , respectively, (2) anomalous volume reduction occurs during the SCO, and (3) volume anomaly and the SCO region are broadened by temperature. All these characteristics arise from $V(P)$ being the weighted average of V_{LS} and V_{HS} (see the SM [64]):

$$V(P) = \left(\frac{\partial G}{\partial P} \right)_T = nV_{LS} + (1 - n)V_{HS}, \quad (2)$$

which clearly indicates that the volume anomaly is directly related to the LS fraction n .

In Figs. 4(d)–4(f), we plot the isothermal bulk modulus $K_T \equiv -V(\partial P/\partial V)_T$ of the MS phase, along with its HS and LS counterparts (K_T^{HS} and K_T^{LS}). For all iron concentrations and all temperatures, $K_T^{HS} < K_T^{LS}$, due to the smaller IFCs between the HS Fe and neighboring atoms [see Fig. 2(b) and 2(c)]. During the SCO, K_T goes through an anomalous softening rather than just shift from K_T^{HS} to K_T^{LS} . This can be understood via Eq. (3) below (see the SM [64])

$$\frac{V}{K_T} = n \frac{V_{LS}}{K_T^{LS}} + (1 - n) \frac{V_{HS}}{K_T^{HS}} + (V_{HS} - V_{LS}) \left(\frac{\partial n}{\partial P} \right)_T, \quad (3)$$

which indicates that the anomaly of K_T mainly arises from $(\partial n/\partial P)_T$. By comparing K_T with $(\partial n/\partial P)_T$ shown in Figs. 3(d)–3(f), one can notice that the peaks of $(\partial n/\partial P)_T$ and the dips of K_T not only align with each other, but are also broadened and smeared by

temperature in the same manner. Likewise, in Figs. 4(g)–4(i), we plot the volumetric thermal expansivity $\alpha \equiv (1/V)(\partial V/\partial T)_P$ of the MS phase, along with its HS and LS counterparts (α_{HS} and α_{LS}). During the SCO, α goes through an anomalous increase rather than just shift from α_{HS} to α_{LS} . This can be understood via Eq. (4) below (see the SM [64])

$$\alpha V = nV_{LS}\alpha_{LS} + (1 - n)V_{HS}\alpha_{HS} - (V_{HS} - V_{LS}) \left(\frac{\partial n}{\partial T} \right)_P, \quad (4)$$

which indicates that the anomaly of α mainly arises from $(\partial n/\partial T)_P$. By comparing α with $(\partial n/\partial T)_P$ shown in Figs. 3(g)–3(i), one can notice that the peaks of α and the dips of $(\partial n/\partial T)_P$ not only align with each other, but are also broadened and smeared by temperature in the same manner. Furthermore, our calculations also indicate that the anomalies of K_T and α are quite significant even at low iron concentration. For $x = 0.125$, K_T drops by 47%, 31%, and 16% [Fig. 4(d)], and α increases to 6.5, 3.1, and 2 times larger [Fig. 4(g)] in the SCO region at $T = 300$, 600, and 1200 K, respectively. When $x = 0.5$, K_T drops by 77%, 61%, and 43% [Fig. 4(e)], and α increases to 21, 8.9, and 4.6 times larger [Fig. 4(h)] at $T = 300$, 600, and 1200 K, respectively.

Next, we compare our theoretical results with experiments for iron concentration $x = 0.65$ by Liu *et al.* [29] and Fu *et al.* [31], and $x = 1$ by Farfan *et al.* [16], Lavina *et al.* [27], and Nagai *et al.* [28]. The Gibbs free energy $G_i(P, T)$ of spin state i ($i = \text{HS}$ or LS) for $x = 0.65$ is obtained by interpolating the results of $x = 0.5$ and $x = 1$ (see the SM [64]); from $G_i(P, T)$, the Gibbs free energy $G(P, T)$ and all thermal parameters of the MS phase can be determined. In Figs. 5(a) and 5(b), compression curves $V(P)$ for $x = 0.65$ and $x = 1$ are shown. In our previous static calculation, theory underestimates the room-temperature equilibrium volume (V_0) by $\sim 4\%$ [32]; in the present calculation with the inclusion of lattice vibration, such underestimate is reduced to $\sim 2\%$. For both iron concentrations, theoretical results are overall in good agreement with experiments. To better examine the volume anomaly, we plot the relative volume difference between $(\text{Mg}_{1-x}\text{Fe}_x)\text{CO}_3$ and MgCO_3 (V_{Mg}) for $x = 0.65$ and $x = 1$ in Figs. 5(c) and 5(d), respectively. The computed and measured $V_{Mg}(P, T)$ [66] are adopted to plot the $(V - V_{Mg})/V_{Mg}$ curves for the theoretical and experimental results, respectively. For $x = 1$ [Fig. 5(d)], all three room-temperature experiments [16, 27, 28] exhibit the same trend and show slight difference: (1) Overall, the SCO starts at as low as 45 GPa and finishes at as high as 60 GPa, (2) HS FeCO_3 is 5–8%

larger (in volume) than MgCO_3 , and LS FeCO_3 is 2–4% smaller than MgCO_3 , and (3) a volume reduction of $\sim 9\%$ occurs in the SCO region. In our calculation for $T = 300$ K (indicated by the blue line), a volume reduction of $\sim 9\%$ occurs in the SCO region 52–62 GPa, in good agreement with experiments. It should be pointed out that four different experiments are adopted for this comparison (three for FeCO_3 ; one for MgCO_3), and each experiment has its own systematic error. As can be observed, the measured FeCO_3 volumes in these experiments differ by $\sim 2\%$. Likewise, the measured MgCO_3 volume, which is used as the reference V_{Mg} for experiments, may also have an uncertainty of $\sim 2\%$. Considering this factor, the apparent discrepancy between the theoretical and experimental results is in fact within the uncertainty of experiments. For $x = 0.65$, [Fig. 5(c)], our calculation is also in good agreement with the experiment by Liu *et al.* [29]. A volume reduction of $\sim 6.5\%$ and the broadening of the SCO region with increasing temperature can be observed in both the theoretical and experimental results. On the other hand, the computed spin-transition pressures and SCO regions are ~ 10 GPa higher and 5–15 GPa wider, respectively, than the experimental results.

In Fig. 6, we compare the computed and measured bulk modulus K_T , volumetric thermal expansivity α , and adiabatic bulk modulus $K_S \equiv -V(\partial P/\partial V)_S$ of $(\text{Mg}_{0.35}\text{Fe}_{0.65})\text{CO}_3$ (see Fig. 8 for the calculation of K_S). Overall, theoretical and experimental results are in agreement. As shown in Figs. 6(a) and 6(b), anomalies of K_T and α observed in the experiment by Liu *et al.* [29] are 25–50% and $\sim 100\%$ larger (in magnitude) than the theoretical results, respectively, despite that theory and experiment give the same volume anomalies of $\sim 6.5\%$ (Fig. 5). The main reason is that the SCO region observed by Liu *et al.* is narrower than the theoretical results, namely, $(\partial n/\partial P)_T$ and $(\partial n/\partial T)_P$ observed by Liu *et al.* have greater magnitudes, leading to greater anomalies in K_T and α , respectively [see Eqs. (3) and (4)]. As to K_S , the theoretical result for $T = 300$ K is in excellent agreement with the room-temperature experiment by Fu *et al.* [31] before the SCO ($P \lesssim 41$ GPa), while the anomaly observed in the experiment is slightly narrower and $\sim 15\%$ larger than the theoretical result. Interestingly, in principle, K_S should be larger than K_T [see later in Eq. (8)], but the measured K_S [Fig. 6(c)] and K_T [Fig. 6(a)] show otherwise. Such inconsistency between different experiments indicates that the uncertainties of experimental results may be larger than they seem.

In Fig. 7, we show our *predictive* calculations for the constant-pressure (C_P) and constant-volume (C_V) heat capacities of $(\text{Mg}_{1-x}\text{Fe}_x)\text{CO}_3$ at high P - T conditions. Their HS/LS counterparts ($C_P^{HS/LS}$ and $C_V^{HS/LS}$) are also plotted. The computed C_P for FeCO_3 ($x = 1$) at $T = 300$ K [Fig. 7(c)] is in good agreement with the room-temperature measurement [67]. For all iron concentrations, the HS state has slightly larger heat capacities than the LS state ($C_P^{HS} > C_P^{LS}$; $C_V^{HS} > C_V^{LS}$), especially at lower temperature. This can be understood via the VDOS of ferromagnesite: HS Fe atoms vibrate at lower frequencies than the LS Fe atoms [Figs. 2(b) and 2(c)]. As the temperature increases to 1200 K, such difference becomes negligible, even for FeCO_3 ($x = 1$) [Figs. 7(c) and 7(f)]. During the SCO, C_P undergoes anomalous increases of $\sim 6\%$, $\sim 24\%$, and $\sim 45\%$ for iron concentrations $x = 0.125$, 0.5 , and 1 , respectively [Figs. 7(a)–7(c)]. Remarkably, the anomaly of C_P retains its magnitude without smearing out at high temperature, in contrast to the anomalies of bulk modulus and thermal expansivity (Figs. 4 and 6). This characteristic of C_P can be understood via Eq. (5) below (see the SM [64]),

$$\begin{aligned} C_P &\equiv T \left(\frac{\partial S}{\partial T} \right)_P \\ &= nC_P^{LS} + (1-n)C_P^{HS} + T(S_{LS} - S_{HS}) \left(\frac{\partial n}{\partial T} \right)_P + (G_{LS} - G_{HS}) \left(\frac{\partial n}{\partial T} \right)_P. \end{aligned} \quad (5)$$

For C_P , the maximum of the anomaly occurs at around the spin phase boundary, namely, when $\Delta G_{LS} \equiv G_{LS} - G_{HS} \approx 0$. Therefore, when C_P reaches its maximum,

$$C_P \approx nC_P^{LS} + (1-n)C_P^{HS} + T(S_{LS} - S_{HS}) \left(\frac{\partial n}{\partial T} \right)_P, \quad (6)$$

which indicates that the maximum anomaly of C_P is mainly determined by $T(\partial n/\partial T)_P$ rather than $(\partial n/\partial T)_P$. Since the smearing of $(\partial n/\partial T)_P$ with increasing temperature [Figs. 3(g)–3(i)] is now compensated by multiplying with T , the anomaly of C_P remains prominent at high temperature. As to C_V [Figs. 7(d)–7(f)], the anomalous increases in the SCO region are significantly smaller than those of C_P ; outside of the SCO region, C_V and C_P are nearly the same. This can be understood via Eq. (7) below

$$C_V \equiv T \left(\frac{\partial S}{\partial T} \right)_V = C_P - TV\alpha^2 K_T, \quad (7)$$

where the term $TV\alpha^2K_T$, also plotted in Figs. 7(d)–7(f), is small outside of the SCO region and exhibits an anomalous increase in the SCO region.

A couple of implications can be drawn from our analysis for the heat capacity C_P . First, among the currently available experiments, the SCO region reported in Ref. 29 by Liu *et al.* is among the narrowest, providing possible upper limits for the magnitudes of $(\partial n/\partial P)_T$ and $(\partial n/\partial T)_P$. Based on the comparison of thermal expansivity α in Fig. 6(b), $(\partial n/\partial T)_P$ observed in Ref. 29 can be twice as large as our theoretical result. Since the anomaly of C_P is determined by $T(\partial n/\partial T)_P$ [Eq. (6)], we estimate that the anomaly of C_P in $(\text{Mg}_{1-x}\text{Fe}_x)\text{CO}_3$ during SCO would be 6–12%, 24–48%, and 45–90% for iron concentration $x = 0.125$, 0.5, and 1, respectively. Such a significant change of C_P during SCO may affect the temperature of subducting slabs. Second, in TR-based experiments, either thermal diffusivity $D \equiv \kappa/\rho C_P$ or thermal effusivity $e \equiv \sqrt{\kappa\rho C_P}$ are measured (ρ is density). To accurately extract thermal conductivity (κ) from TR-based experiments, accurate C_P is a necessary input. In practice, since C_P at high P – T conditions are not easily available, estimated C_P are often adopted without considering the anomaly of C_P during SCO [46, 47]. Our results thus call for further examinations of thermal conductivities extracted from TR-based experiments, given the significant anomaly of C_P accompanying SCO.

With C_P and C_V obtained, a few more thermal parameters can be determined, including thermodynamic Grüneisen parameter γ , adiabatic bulk modulus K_S , and bulk sound velocity V_Φ . In general, the thermodynamic Grüneisen parameter $\gamma \equiv V\alpha K_T/C_V$ of a material marginally changes with pressure and temperature, as can be observed in pure HS and LS $(\text{Mg,Fe})\text{CO}_3$ [Figs. 8(a)–8(c)]. In the SCO region, however, γ exhibits an anomalous increase, which smears out as the temperature increases, similar to thermal expansivity α . Noticeably, even at low iron concentration $x = 0.125$, anomalies of γ are still prominent: $\sim 260\%$, $\sim 116\%$, and $\sim 60\%$ at $T = 300$, 600, and 1200 respectively [Fig. 8(a)]. For adiabatic bulk modulus K_S [Figs. 8(d)–8(f)], its anomalous softening is similar to that of the isothermal bulk modulus K_T [Figs. 4(d)–4(f)], given that

$$K_S \equiv -V \left(\frac{\partial P}{\partial V} \right)_S = K_T \frac{C_P}{C_V} = K_T(1 + \gamma\alpha T). \quad (8)$$

Outside of the SCO region, $C_P \approx C_V$ (Fig. 7), therefore, $K_S \approx K_T$; in the SCO region,

$1 < C_P/C_V \lesssim 1.5$ (Fig. 7), so the dips of K_S are slightly shallower than those of K_T . Since the bulk sound velocity $V_\Phi \equiv \sqrt{K_S/\rho}$, the anomaly of V_Φ resembles that of K_S [Figs. 8(g)–8(i)]. Based on the phonon gas model, thermal conductivity $\kappa = \frac{1}{3}C_P V_\Phi l = \frac{1}{3}C_P V_\Phi^2 \tau$, where l and τ are the phonon mean free path and phonon scattering time, respectively. Anomalies of C_P and V_Φ in the SCO region thus directly contribute to the anomalous change of thermal conductivity (see Ref. 68 for a discussion on ferropericline). Calculations for κ and τ from the first principles, however, are beyond the scope of this paper.

IV. CONCLUSION

In this work, we perform first-principles LDA+ U_{sc} calculations to study the iron spin crossover and thermal properties of ferromagnesite ($\text{Mg}_{1-x}\text{Fe}_x$) CO_3 up to high pressure ($P = 100$ GPa) and temperature ($T = 1200$ K). Our calculations show that throughout a wide range of iron concentration ($0 < x \leq 1$), the spin phase diagram of ferromagnesite remains nearly the same. The spin transition pressure P_t , the width of the SCO region, and their increase with temperature are barely affected by iron concentration. Our calculations also show that the thermal properties of ($\text{Mg}_{1-x}\text{Fe}_x$) CO_3 are drastically altered by SCO, including anomalous reduction of volume, anomalous softening of bulk modulus, and anomalous increase of thermal expansivity. These results are overall in good agreement with experiments. Our calculations also predict anomalous increases of heat capacity and thermodynamic Grüneisen parameter during SCO. Remarkably, the anomaly of constant-pressure heat capacity C_P remains prominent at high temperature without smearing out, in contrast to the anomalies of bulk modulus, thermal expansivity, and bulk sound velocity. This result suggests significant change of thermal conductivity during SCO; it also calls for further examinations of the results obtained from TR-based experiments, as inaccurate C_P has been adopted to extract thermal conductivity. Our results further suggest that SCO may significantly affect the thermal properties and temperature of subducting slabs, given that several minerals abundant in subducting slabs undergo SCO in the lower-mantle pressure range, including ferromagnesite, the NAL, and the CF phases.

Acknowledgments This work is supported by the Ministry of Science and Technology of Taiwan under Grants No. MOST 107-2112-M-008-022-MY3 and 107-2119-M-009-009-MY3. Z.W. is supported by National Natural Science Foundation of China (41925017).

Calculations were performed primarily at National Center for High-performance Computing (NCHC) of Taiwan and partly at the Supercomputing Center of University of Science and Technology of China.

- [1] *Carbon in Earth*, edited by R. M. Hazen, A. P. Jones, and J. A. Baross, special issue of Rev. Mineral. Geochem. **75** (2013).
- [2] *Carbon in Earth's Interior*, edited by C. E. Manning, J.-F. Lin, and W. L. Mao, Geophysical Monograph Series Vol. 249 (2020).
- [3] M. Isshiki, T. Irifune, K. Hirose, S. Ono, Y. Ohishi, T. Watanuki, E. Nishibori, M. Takata, and M. Sakata, Nature **427**, 60 (2004).
- [4] J. Liu, J.-F. Lin, and V. Prakapenka, Sci. Rep. **5**, 7640 (2015).
- [5] V. Cerantola, E. Bykova, I. Kupenko¹, M. Merlini, L. Ismailova, C. McCammon, M. Bykov, A. I. Chumakov, S. Petitgirard, I. Kantor, V. Svitlyk, J. Jacobs, M. Hanfland, M. Mezouar, C. Prescher, R. Ruffer, V. B. Prakapenka, and L. Dubrovinsky, Nat. Commun. **8**, 15960 (2017).
- [6] E. Boulard, A. Gloter, A. Corgne, D. Antonangeli, A.-L. Auzende, J.-P. Perrillat, F. Guyot, and G. Fiquet, Proc. Natl. Acad. Sci. U.S.A. **108**, 5184 (2011).
- [7] E. Boulard, D. Pan, G. Galli, Z. Liu, and W. L. Mao, Nat. Commun. **6**, 6311 (2015).
- [8] M. Merlini, M. Hanfland, A. Salamat, S. Petitgirard, and H. Muller, Ame. Mineral. **100**, 2001 (2015).
- [9] E. Boulard, F. Guyot, and G. Fiquet, in *Carbon in Earth's Interior*, edited by C. E. Manning, J.-F. Lin, and W. L. Mao, Geophysical Monograph Series Vol. 249 (2020).
- [10] A. R. Oganov, S. Ono, Y. Ma, C. W. Glass, and A. Garcia, Earth Planet. Sci. Lett. **273**, 38 (2008).
- [11] C. J. Pickard and R. J. Needs, Phys. Rev. B **91**, 104101 (2015).
- [12] Z. Li and S. Stackhouse, Earth Planet. Sci. Lett. **531**, 115959 (2020).
- [13] J. Tsuchiya, R. Nishida, and T. Tsuchiya, Minerals **10**, 54 (2020).
- [14] A. Mattila, T. Pytkkanen, J-P Rueff, S. Huotari, G. Vanko, M. Hanfland, M. Lehtinen, and K. Hamalainen, J. Phys. Condens. Matter **19**, 386206 (2007).
- [15] V. Cerantola, C. McCammon, I Kupenko, I. Kantor, C. Marini, M. Wilke, L. Ismailova, N. Solopova, A. Chumakov, S. Pascarelli, and L. Dubrovinsky, Am. Min. **100**, 2670 (2015).

- [16] G. Farfan, S. Wang, H. Ma, R. Caracas, and W. L. Mao *Am. Min.* **97**, 1421 (2012).
- [17] J.-F. Lin, J. Liu, C. Jacobs, and V. Prakapenka, *Am. Min.* **97**, 583 (2012).
- [18] J. Muller, S. Speziale, I. Efthymiopoulos, S. Jahn, and M. Koch-Muller, *Am. Min.* **101**, 2638 (2016).
- [19] J. Muller, I. Efthymiopoulos, S. Jahn, and M. Koch-Muller, *Eur. J. Mineral.* **29**, 785 (2017).
- [20] C. Weis, C. Sternemann, V. Cerantola, C. J. Sahle, G. Spiekermann, M. Harder, Y. Forov, A. Kononov, R. Sakrowski, H. Yavas, M. Tolan, and M. Wilke, *Sci. Rep.* **7**, 16526 (2017).
- [21] K. H. Chao and W. P. Hsieh, *J. Geophys. Res. Solid Earth* **124**, 1388 (2019).
- [22] S. S. Lobanov, A. F. Goncharov, and K. D. Litasov, *Am. Min.* **100**, 1059 (2015).
- [23] S. S. Lobanov, N. Holtgrewe, and A. F. Goncharov, *Earth Planet. Sci. Lett.* **449**, 20 (2016).
- [24] M. N. Taran, J. Muller, A. Friedrich, and M. Koch-Muller, *Phys. Chem. Minerals* **44**, 537 (2017).
- [25] B. Lavina, P. Dera, R. T. Downs, V. Prakapenka, M. Rivers, S. Sutton, and M. Nicol, *Geophys. Res. Lett.* **36**, L23306 (2009).
- [26] B. Lavina, P. Dera, R. T. Downs, O. Tschauner, W. Yang, O. Shebanova, and G. Shen, *High Press. Res.* **30**, 224 (2010).
- [27] B. Lavina, P. Dera, R. T. Downs, W. Yang, S. Sinogeikin, Y. Meng, G. Shen, and D. Schifer, *Phys. Rev. B* **82**, 064110 (2010).
- [28] T. Nagai, T. Ishido, Y. Seto, D. Nishio-Hamane, N. Sata, and K. Fujino, *J. Phys. Conf. Ser.* **215**, 012002 (2010).
- [29] J. Liu, J.-F. Lin, Z. Mao, and V. Prakapenka, *Am. Min.* **99**, 84 (2014).
- [30] M. Stekiel, T. Nguyen-Thanh, S. Chariton, C. McCammon, A. Bosak, W. Morgenroth, V. Milman, K. Refson, B. Winkler, *Phys. Earth Planet. In.* **271**, 57 (2017).
- [31] S. Fu, J. Yang, and J.-F. Lin *Phys. Rev. Lett.* **118**, 036402 (2017).
- [32] H. Hsu and S. C. Huang, *Phys. Rev. B* **94**, 060404(R) (2016).
- [33] H. Hsu, K. Umemoto, Z. Wu, and R. M. Wentzcovitch, *Rev. Mineral Geochem.* **71**, 169 (2010).
- [34] R. M. Wentzcovitch, H. Hsu, and K. Umemoto, *Eur. J. Mineral.* **24**, 851 (2012).
- [35] J.-F. Lin, S. Speziale, Z. Mao, and H. Marquardt, *Rev. Geophys.* **51**, 244 (2013).
- [36] J. Badro, *Annu. Rev. Earth Planet. Sci.* **42**, 231 (2014).
- [37] C. Huang, W. Leng, and Z. Wu, *Earth Planet. Sci. Lett.* **423**, 173 (2015).
- [38] Z. Wu and R. M. Wentzcovitch *Proc. Natl. Acad. Sci.* **111**, 10468 (2014).

- [39] Y. Wu, X. Wu, J.-F. Lin, C. A. McCammond, Y. Xiao, P. Chow, V. B. Prakapenka, T. Yoshino, S. Zhai, and S. Qin, *Earth Planet. Sci. Lett.* **434**, 91 (2016).
- [40] S. S. Lobanov, H. Hsu, J.-F. Lin, T. Yoshino, and A. F. Goncharov, *J. Geophys. Res. Solid Earth*, **122**, 3565 (2017).
- [41] H. Hsu, *Phys. Rev. B* **95**, 020406(R) (2017).
- [42] Y. Wu, F. Qin, X. Wu, H. Huang, C. A. McCammon, T. Yoshino, S. Zhai, Y. Xiao, and V. B. Prakapenka, *J. Geophys. Res. Solid Earth* **122**, 5935 (2017).
- [43] J. Liu, Q. Hu, W. Bi, L. Yang, Y. Xiao, P. Chow, Y. Meng, V. B. Prakapenka, H.-K. Mao, and W. L. Mao, *Nat. Commun.* **10**, 153 (2019).
- [44] B. G. Jang, J. Liu, Q. Hu, K. Haule, H.-K. Mao, W. L. Mao, D. Y. Kim, and J. H. Shim *Phys. Rev. B* **100**, 014418 (2019).
- [45] K. Ohta, T. Yagi, K. Hirose, and Y. Ohishi, *Earth Planet. Sci. Lett.* **465**, 29 (2017).
- [46] W.-P. Hsieh, F. Deschamps, T. Okuchi, and J.-F. Lin *Proc. Natl. Acad. Sci.* **115**, 4099 (2018).
- [47] W.-P. Hsieh, F. Deschamps, T. Okuchi, and J.-F. Lin *J. Geophys. Res. Solid Earth* **122**, 4900 (2017).
- [48] Y. Okuda, K. Ohta, R. Sinmyo, K. Hirose, T. Yagi, and Y. Ohishi, *Earth Planet. Sci. Lett.* **520**, 188 (2019).
- [49] A. Hasegawa, T. Yagi, and K. Ohta, *Rev. Sci. Instrum.* **90**, 074901 (2019).
- [50] P. Jiang, X. Qian, and R. Yang, *J. Appl. Phys.* **124**, 161103 (2018).
- [51] Z. Wu, J. F. Justo, C. R. S. da Silva, S. de Gironcoli, and R. M. Wentzcovitch, *Phys. Rev. B* **80**, 014409 (2009).
- [52] P. Giannozzi, O. Andreussi, T. Brumme, O. Bunau, M. Buongiorno Nardelli, M. Calandra, R. Car, C. Cavazzoni, D. Ceresoli, M. Cococcioni, N. Colonna, I. Carnimeo, A. Dal Corso, S. de Gironcoli, P. Delugas, R. A. DiStasio Jr., A. Ferretti, A. Floris, G. Fratesi, G. Fugallo, R. Gebauer, U. Gerstmann, F. Giustino, T. Gorni, J. Jia, M. Kawamura, H.-Y. Ko, A. Kokalj, E. Kucukbenli, M. Lazzeri, M. Marsili, N. Marzari, F. Mauri, N. L. Nguyen, H.-V. Nguyen, A. Otero-de-la-Roza, L. Paulatto, S. Ponce, D. Rocca, R. Sabatini, B. Santra, M. Schlipf, A. P. Seitsonen, A. Smogunov, I. Timrov, T. Thonhauser, P. Umari, N. Vast, X. Wu, and S. Baroni, *J. Phys.: Condens. Matter* **29**, 465901 (2017).
- [53] D. Vanderbilt *Phys. Rev. B* **41**, 7892(R) (1990).
- [54] M. Cococcioni and S. de Gironcoli, *Phys. Rev. B* **71**, 035105 (2005).

- [55] H. J. Kulik, M. Cococcioni, D. A. Scherlis, and N. Marzari, *Phys. Rev. Lett.* **97**, 103001 (2006).
- [56] B. Himmetoglu, R. M. Wentzcovitch, and M. Cococcioni, *Phys. Rev. B* **84**, 115108 (2011).
- [57] B. Himmetoglu, A. Floris, S. Gironcoli, and M. Cococcioni, *Int. J. Quantum Chem.* **114**, 14 (2014).
- [58] H. Hsu, K. Umemoto, P. Blaha, and R. M. Wentzcovitch, *Earth Planet. Sci. Lett.* **294**, 19 (2010).
- [59] H. Hsu, P. Blaha, M. Cococcioni, and R. M. Wentzcovitch, *Phys. Rev. Lett.* **106**, 118501 (2011).
- [60] H. Hsu, Y. G. Yu, and R. M. Wentzcovitch, *Earth Planet. Sci. Lett.* **359–360**, 34 (2012).
- [61] Y. G. Yu, H. Hsu, M. Cococcioni, and R. M. Wentzcovitch, *Earth Planet. Sci. Lett.* **331–332**, 1 (2012).
- [62] H. Hsu and R. M. Wentzcovitch, *Phys. Rev. B* **90**, 195205 (2014).
- [63] A. Togo and I. Tanaka, *Scr. Mater.* **108**, 1 (2015). See also <http://phonopy.github.io/phonopy/>
- [64] See Supplemental Material at <http://inserted.by.publisher> for the thermodynamic model and derivations of thermal parameters.
- [65] T. Qin, Q. Zhang, R. M. Wentzcovitch, and K. Umemoto, *Comput. Phys. Commun.* **237**, 199 (2019).
- [66] K. D. Litasova, Y. Fei, E. Ohtani, T. Kuribayashi, and K. Funakoshic, *Phys. Earth Planet. Inter.* **168**, 191 (2008).
- [67] R. A. Robie, H. T. Haselton, Jr., and B. S. Hemingway, *Am. Min.* **69**, 349 (1984).
- [68] Z. Wu, *Am. Min.* **103**, 1953 (2018).

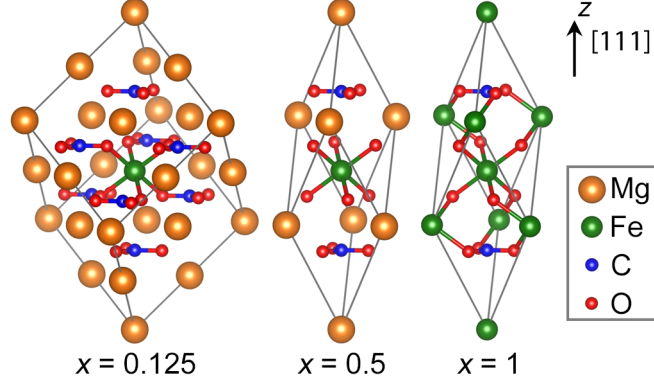


FIG. 1. Atomic structures of ferromagnesite $(\text{Mg}_{1-x}\text{Fe}_x)\text{CO}_3$ for $x = 0.125$ (40-atom supercell) and $x = 0.5$ and 1 (10-atom cell). The end member FeCO_3 ($x = 1$) crystallizes in calcite structure ($R\bar{3}c$ symmetry), same as MgCO_3 ($x = 0$, not shown). In this graph, the $[111]$ direction is aligned with the z axis.

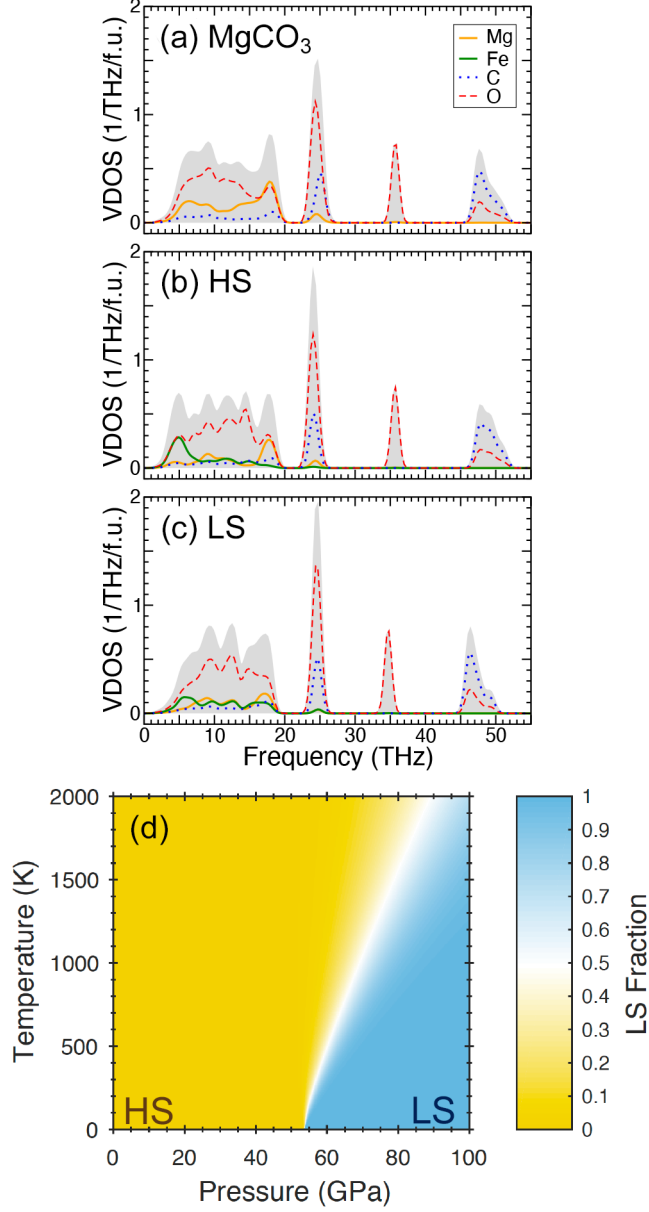


FIG. 2. Vibrational density of states of ferromagnesite $(\text{Mg}_{1-x}\text{Fe}_x)\text{CO}_3$ at volume $V = 37.01 \text{ \AA}^3/\text{f.u.}$ for (a) $x = 0$ and (b,c) $x = 0.5$ in the HS and LS states, respectively. In panels (a)–(c), the gray shades denote the total VDOS; the lines denote the projected VDOS onto the Mg, Fe, C, and O atoms. Also, $1 \text{ THz} = 33.356 \text{ cm}^{-1}$. (d) Spin phase diagram of $(\text{Mg}_{0.5}\text{Fe}_{0.5})\text{CO}_3$; the fraction of LS iron is indicated by color.

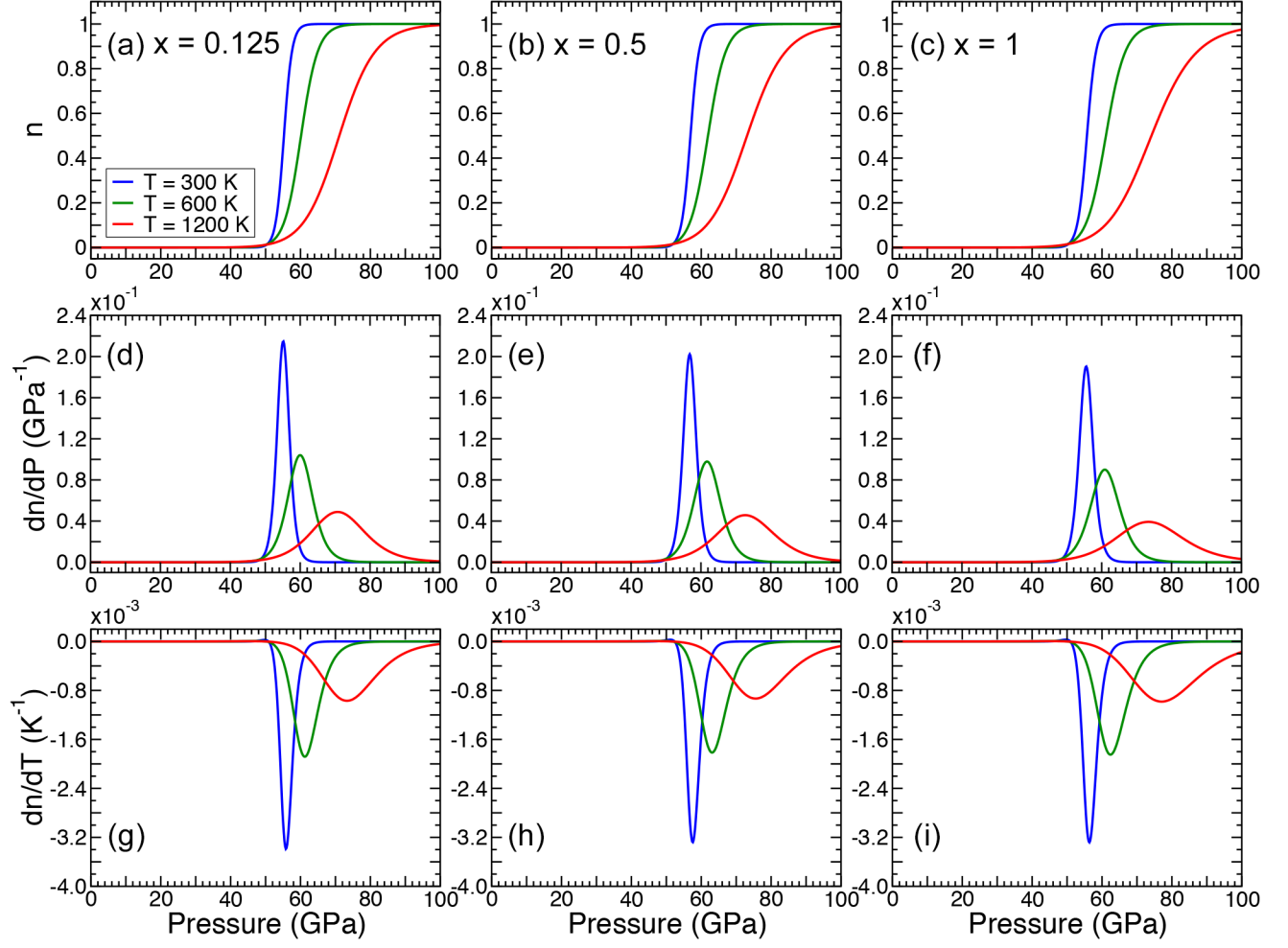


FIG. 3. (a–c) Fractions of LS iron ($n \equiv n_{LS}$) in $(\text{Mg}_{1-x}\text{Fe}_x)\text{CO}_3$ at various temperatures for $x = 0.125, 0.5$, and 1 , respectively; (d–f) $\partial n/\partial P$ and (g–i) $\partial n/\partial T$ for the Fe concentrations and temperatures considered in panels (a)–(c).

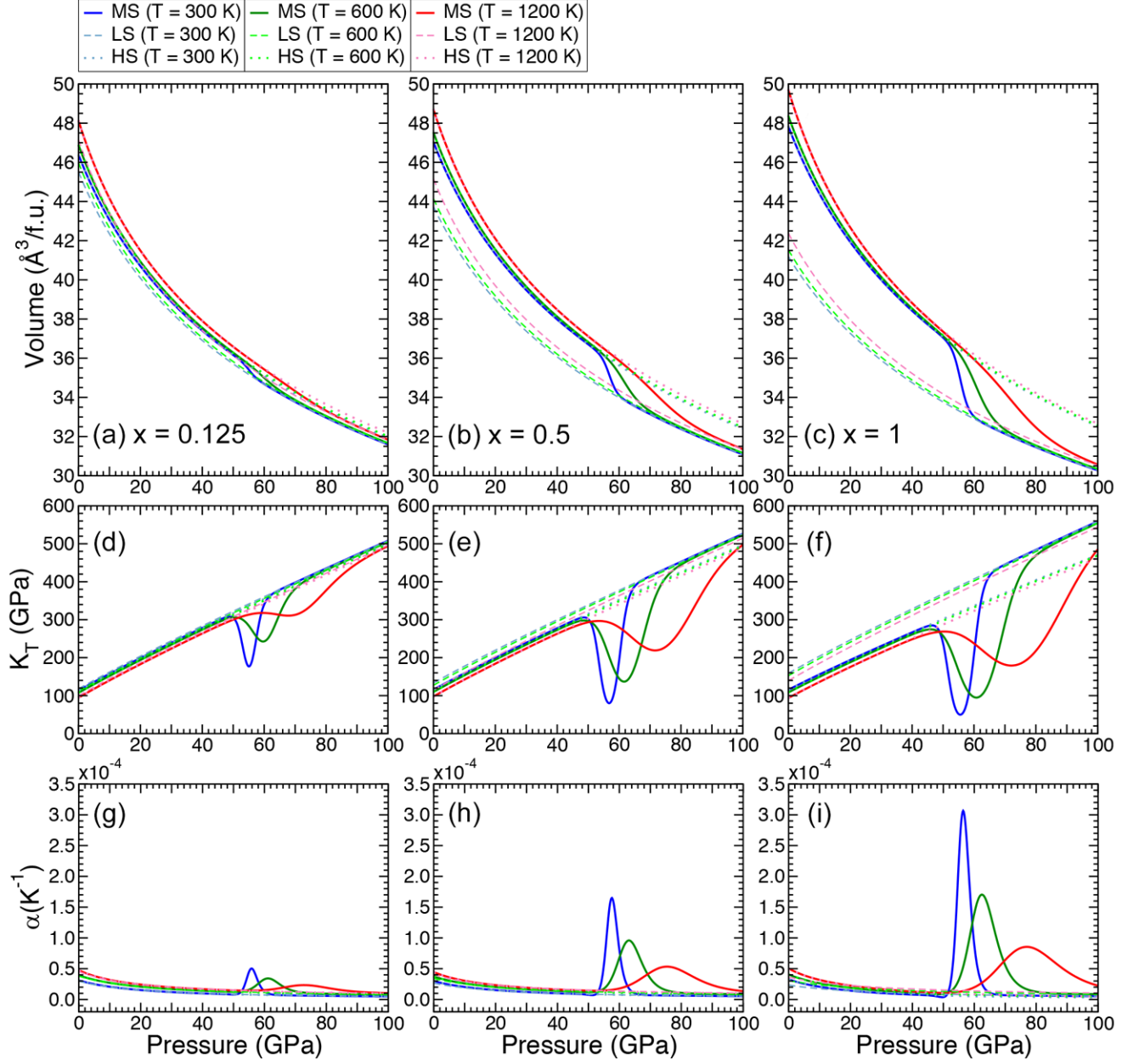


FIG. 4. (a–c) Compression curves $V(P)$, (d–f) isothermal bulk modulus K_T , and (g–i) volumetric thermal expansivity α of $(\text{Mg}_{1-x}\text{Fe}_x)\text{CO}_3$ for $x = 0.125, 0.5$, and 1 , respectively. Solid, dotted, and dashed lines denote our theoretical results for the MS, HS, and LS states, respectively

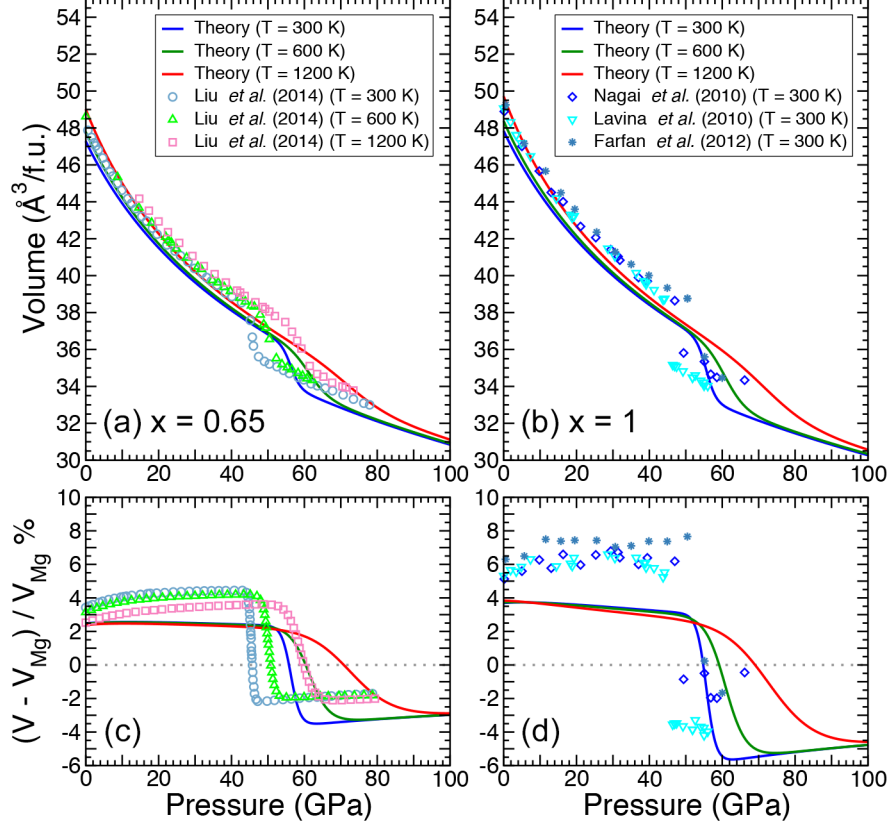


FIG. 5. (a,b) Compression curves of $(\text{Mg}_{1-x}\text{Fe}_x)\text{CO}_3$, and (c,d) relative volume differences between $(\text{Mg}_{1-x}\text{Fe}_x)\text{CO}_3$ and MgCO_3 (V_{Mg}) for $x = 0.65$ and 1. Solid lines denote our theoretical results; symbols denote experimental results [16, 27–29].

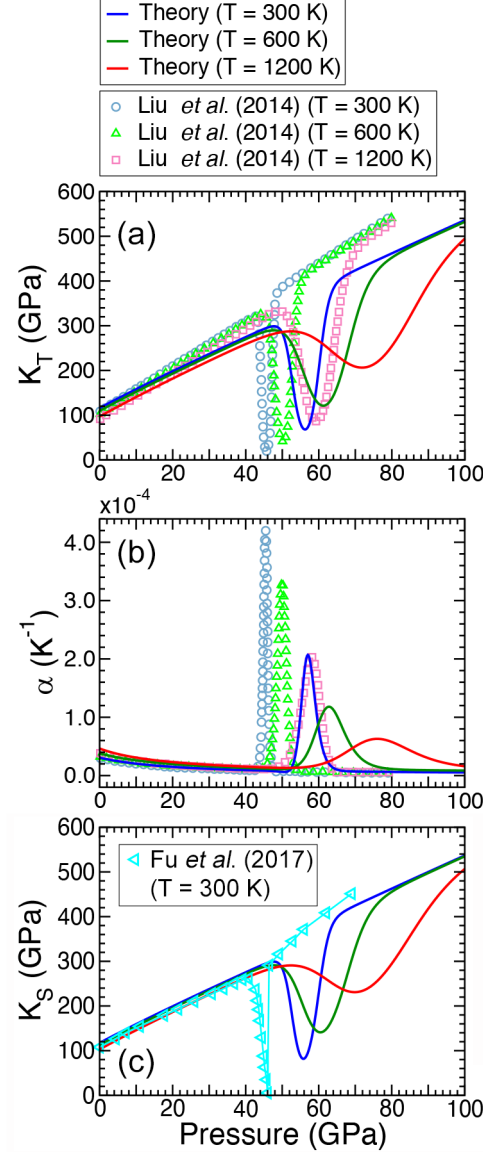


FIG. 6. (a) Isothermal bulk modulus K_T , (b) volumetric thermal expansivity α , and (c) adiabatic bulk modulus K_S of $(\text{Mg}_{0.35}\text{Fe}_{0.65})\text{CO}_3$. Solid lines denote our theoretical results; symbols denote experimental results [29, 31].

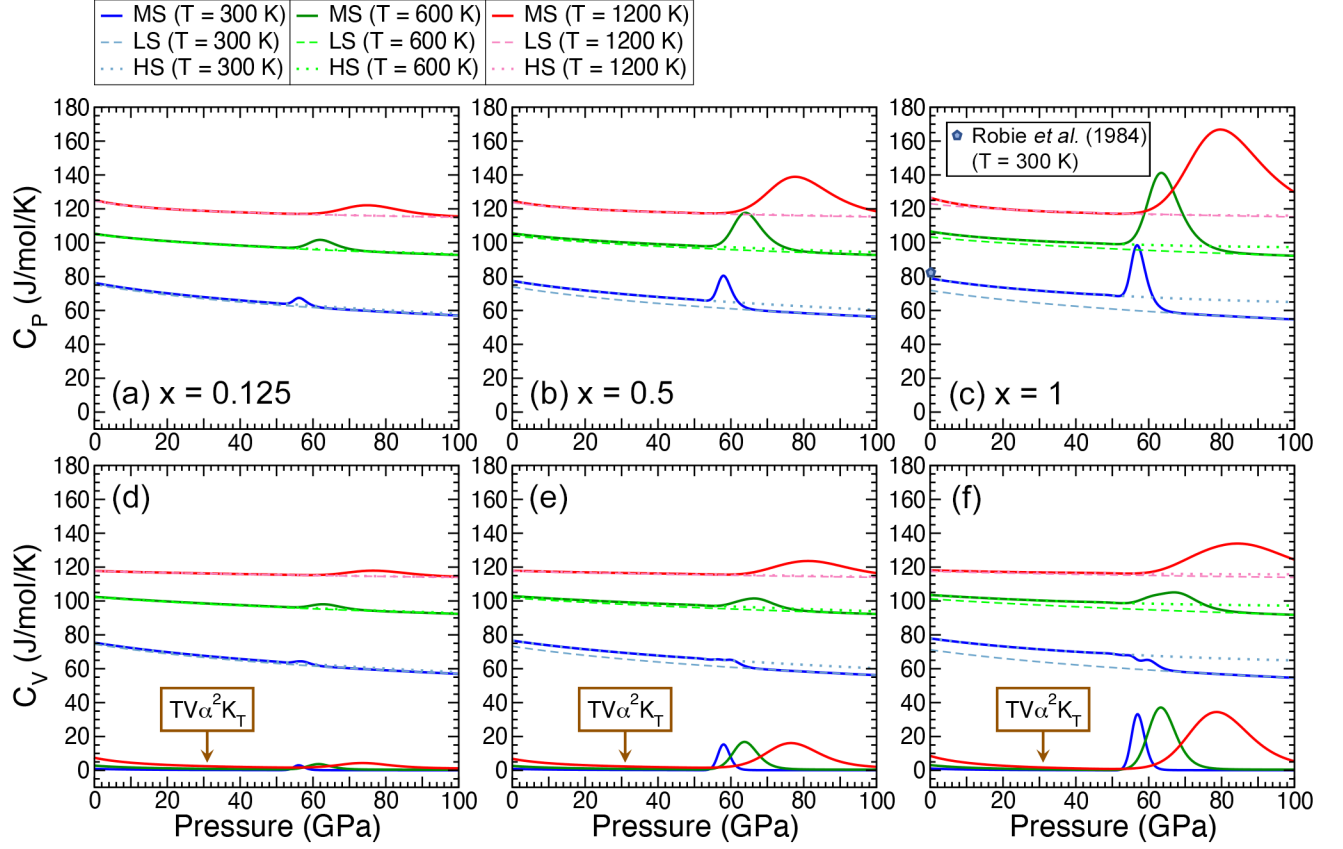


FIG. 7. (a–c) Constant-pressure (C_P) and (d–f) constant-volume (C_V) heat capacities of $(\text{Mg}_{1-x}\text{Fe}_x)\text{CO}_3$ for $x = 0.125, 0.5$, and 1 , respectively. The differences between C_P and C_V , i.e. $TV\alpha^2 K_T$, are also shown in panels (d)–(f). Solid, dotted, and dashed lines denote our theoretical results for the MS, HS, and LS states, respectively; symbols in panel (c) denote experimental results [67].

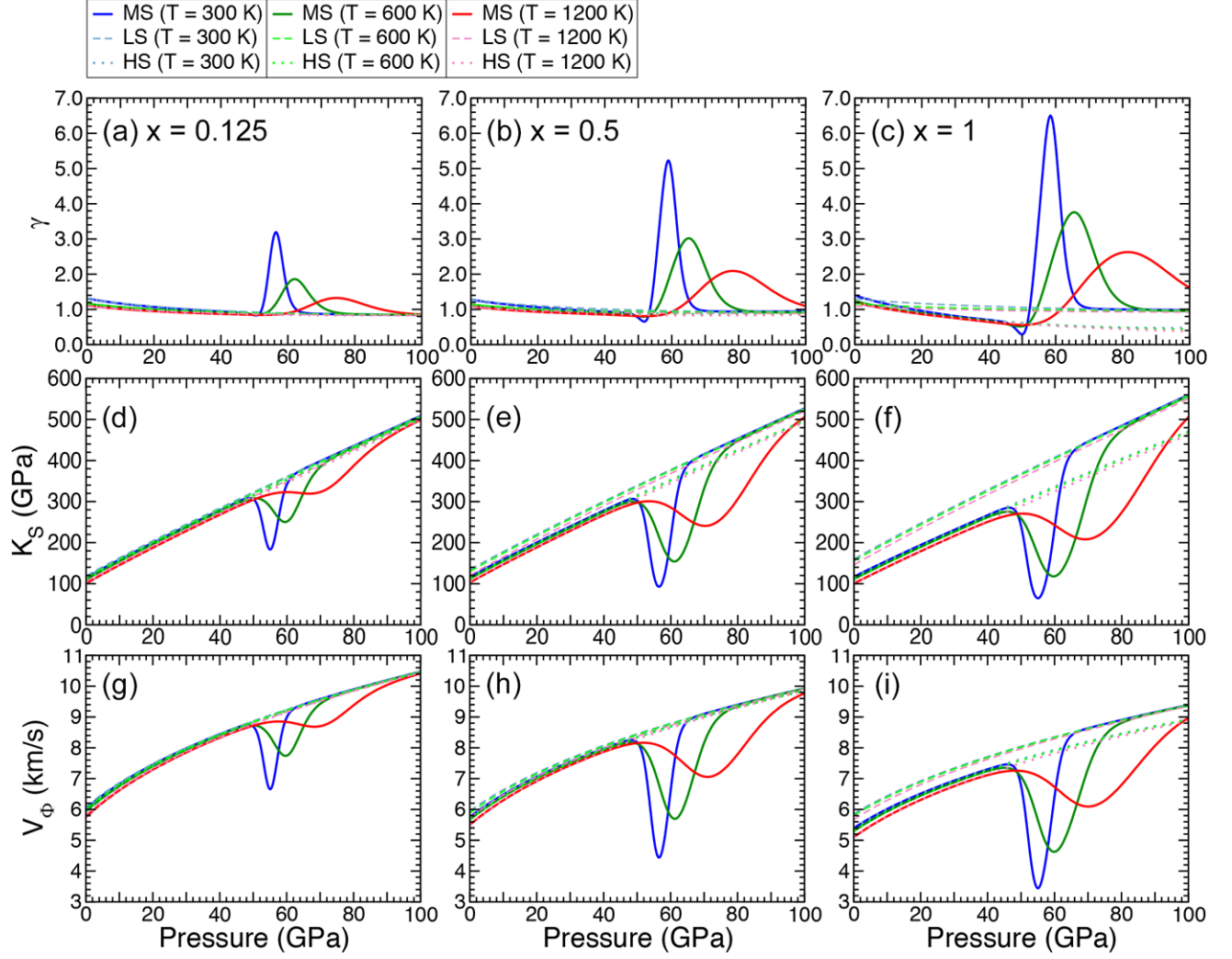


FIG. 8. (a–c) Thermodynamic Grüneisen parameter γ , (d–f) adiabatic bulk modulus K_S , and (g–i) bulk sound velocity V_Φ of $(\text{Mg}_{1-x}\text{Fe}_x)\text{CO}_3$ for $x = 0.125$, 0.5 , and 1 , respectively. Solid, dotted, and dashed lines denote our theoretical results for the MS, HS, and LS states, respectively.